THE *SPITZER SPACE TELESCOPE* FIRST-LOOK SURVEY: KPNO MOSAIC-1 *R*-BAND IMAGES AND SOURCE CATALOGS

Dario Fadda,[1] Buell T. Jannuzi,[2] Alyson Ford,[2] and Lisa J. Storrie-Lombardi[1]

ABSTRACT

We present *R*-band images covering more than 11 square degrees of sky that were obtained in preparation for the *Spitzer Space Telescope* First-Look Survey (FLS). The FLS was designed to characterize the mid-infrared sky at depths 2 orders of magnitude deeper than previous surveys. The extragalactic component is the first cosmological survey done with *Spitzer*. Source catalogs extracted from the *R*-band images are also presented. The *R*-band images were obtained using the Mosaic-1 camera on the 4 m Mayall Telescope of the Kitt Peak National Observatory. Two relatively large regions of the sky were observed to modest depth: the main FLS extragalactic field ($17^h18^m00^s$, $+59°30'00\!\!''.0$ [J2000]; $l = 88°.3$, $b = +34°.9$) and the ELAIS-N1 field ($16^h10^m01^s$, $+54°30'36\!\!''.0$; $l = 84°.2$, $b = +44°.9$). While both these fields were in early plans for the FLS, only a single deep-pointing test observation was made at the ELAIS-N1 location. The larger Legacy program SWIRE will include this region among its surveyed areas. The data products of our KPNO imaging (images and object catalogs) are made available to the community through the World Wide Web (via the *Spitzer* Science Center and NOAO Science Archive). The overall quality of the images is high. The measured positions of sources detected in the images have rms uncertainties in their absolute positions on the order of $0\!\!''.35$ with possible systematic offsets on the order of $0\!\!''.1$, depending on the reference frame of comparison. The relative astrometric accuracy is much better than 1/10 of an arcsecond. Typical delivered image quality in the images is $1\!\!''.1$ full width at half-maximum. The images are relatively deep, since they reach a median 5 σ depth limiting magnitude of $R = 25.5$ (Vega) as measured within a 1.35 FWHM aperture, for which the signal-to-noise ratio (S/N) is maximal. Catalogs have been extracted with SExtractor, using thresholds in area and flux for which the number of false detections is below 1% at $R = 25$. Only sources with S/N > 3 have been retained in the final catalogs. Comparing the galaxy number counts from our images with those of deeper *R*-band surveys, we estimate that our observations are 50% complete at $R = 24.5$. These limits in depth are sufficient to identify a substantial fraction of the infrared sources that will be detected by *Spitzer*.

Key words: catalogs — galaxies: photometry

1. INTRODUCTION

One of the main advantages of the *Spitzer Space Telescope* (formerly known as the *Space Infrared Telescope Facility*, *SIRTF*; Gallagher et al. 2003) is the possibility to make extragalactic surveys of large regions of the sky in a relatively short time covering wavelengths from the near to the far-infrared with the instruments IRAC (Fazio et al. 1998) and MIPS (Rieke et al. 1996). Compared with *Spitzer*'s predecessors (e.g., *IRAS*, Soifer et al. 1983; *ISO*, Kessler et al. 1996), there are improvements in the detectors (number of pixels and better responsivity), the collecting area of the primary mirror (85 cm diameter), and Sun-Earth-Moon avoidance constraints due to *Spitzer*'s heliocentric orbit. *Spitzer* can also make observations simultaneously in multiple bands (with IRAC, 3.6 and 4.5 or 5.8 and 8 μm; with MIPS 24, 70, and 160 μm).

Many extragalactic surveys are already scheduled with *Spitzer* as Legacy programs (SWIRE, Lonsdale et al. 2003; GOODS, Dickinson & Giavalisco 2003) or as observations by the Instrument Teams (wide, deep, and ultraDeep *Spitzer* surveys, which will cover regions such as the Boötes field of the NOAO Deep Wide-Field Survey, the Groth strip, the Lockman Hole, XMM-Deep, and so on; see, e.g., Dole et

2001). The First-Look Survey (FLS) utilizes 112 hours of Director's Discretionary Time on *Spitzer* and includes extragalactic, Galactic, and ecliptic components.[3] These data will be available to all observers when the *Spitzer* Science Archive opens in 2004 May. The purpose of the FLS is to characterize the mid-infrared sky at previously unexplored depths and make these data rapidly available to the astronomical community. The extragalactic component comprises a 4 deg^2 survey with IRAC and MIPS near the north ecliptic pole centered on J1718+5930. These observations were executed on 2003 December 1–11.

To fully exploit the *Spitzer* FLS data, we have obtained ancillary surveys at optical (this paper) and radio (Condon et al. 2003) wavelengths. Given the modest spatial resolution of the *Spitzer* imagers (the point-spread function is large, especially in the mid- and far-IR, e.g., $5\!\!''.7$ FWHM for the 24 μm channel), the first problem to solve for the infrared sources detected by *Spitzer* will be to associate these sources with an optical counterpart, when possible. This will then allow the higher spatial resolution of the available optical images to assist with the source classification (e.g., as stars, galaxies, or QSOs) and enable targeting of subsets of the sources for spectroscopy with optical or near-infrared spectrographs. Since many of the infrared sources that will be detected by *Spitzer* will be dust-obscured galaxies with faint optical counterparts, the complementary optical imaging must be relatively deep.

---

[1] *Spitzer* Science Center, California Institute of Technology, Mail code 220-6, 1200 East California Boulevard, Pasadena, CA 91125.

[2] National Optical Astronomy Observatory, 950 North Cherry Avenue, Tucson, AZ 85719.

[3] See the FLS Web site, at http://ssc.spitzer.caltech.edu/fls.

TABLE 1
Main Features of the Filter Used in the
Mosaic-1 Observations

Feature	Value
Filter..	R
KPNO ID	R Harris k1004
$\lambda_{\rm eff}$..	6440 Å
FWHM	1510 Å
Peak throughput......................	86.2%

Although a deep multiwavelength optical survey would be more useful, allowing one to compute photometric redshifts (e.g., the NOAO Deep Wide-Field Survey; Jannuzi & Dey 1999; Brown et al. 2003), the task of deeply covering a large region of sky in a homogeneous manner is quite time-consuming. Therefore, for the initial optical ancillary survey we chose to observe the entire field in the R band. NOAO provided four nights of Director's Discretionary Time on the KPNO 4 m in 2000 May for this survey. We have limited multiwavelength optical observations to the central portion of the FLS field. The Sloan Digital Sky Survey (SDSS) included the FLS field in their early-release observations (Stoughton et al. 2002), and mosaics and catalogs for the region are now also available (Hogg et al. 2004).

In this paper, we present the R-band optical observations made with the Mosaic-1 camera on the Mayall Telescope of Kitt Peak National Observatory. Centered on the main FLS field, a region 9.4 square degrees in area was imaged. In addition, 2.3 square degrees covering field N1 of the European Large Area *ISO* Survey (ELAIS; Oliver et al. 2000) were also observed. Although originally the ELAIS-N1 field was planned to be part of the FLS program, the FLS observations of the ELAIS-N1 field have now been revised to a very deep $10'' \times 10''$ pointing to evaluate the confusion limits of the MIPS instrument. The remainder of the ELAIS-N1 field will now be imaged as part of a larger survey in this region, a portion of the SWIRE *Spitzer* Legacy Survey (Lonsdale et al. 2003).

In § 2, we review the overall observing strategy and describe the Mosaic-1 observations. In § 3, we discuss the techniques used in the data reduction, including the astrometric and photometric calibration of the images. We describe in § 4 the data products made publicly available. We detail in § 5 the criteria used to detect, classify, and photometrically measure objects in the images. Section 5 also includes a description of the information available in our catalogs. In section 6, we examine the quality of the imaging data by comparing them with other available data sets. Finally, a brief summary is given in § 7.

2. OBSERVATIONS

The optical observations of the FLS region (centered at $17^{\rm h}18^{\rm m}00^{\rm s}$, $+59°30'00''$; J2000) and of the ELAIS-N1 region (centered at $16^{\rm h}10^{\rm m}01^{\rm s}$, $+54°30'36''$; see Oliver et al. 2000) were carried out using the Mosaic-1 camera on the 4 m Mayall Telescope at KPNO. The camera comprises eight thinned, back-illuminated SITe 2048×4098 CCDs with a projected pixel size of $0''258$ (Muller et al. 1998). The eight CCDs are physically separated by gaps with widths of approximately $14''$ and $15''5$ along the right ascension and declination directions, respectively. The full field of view of the camera is therefore $36' \times 36'$, with a filling factor of 97%. Observations were performed using the Harris set Kron-Cousins R-band filter, the main features of which are summarized in Table 1.

The transmission curve of the filter is shown in Figure 1 together with the resulting modifications that would be introduced by the corrector and camera optics, the CCD quantum efficiency, and atmospheric extinction.

For organizational purposes we chose to divide the proposed FLS survey region into 30 subfields, each roughly the size of an individual Mosaic-1 pointing. The coordinates of these subfields are listed in Table 2. During our observing run we were able to complete observations for 26 of these subfields. We similarly divided the ELAIS-N1 field into 12 subfields, but we only completed observations for five of these. Each subfield was observed for a minimum of three 10 minute exposures. In practice, some images were not suitable (poor seeing, flat-fielding problem, or some other defect) and were not included in the final co-added or "stacked" images we are providing to the community. The fourth column of Table 2 lists the number of exposures that were obtained and included in the stacked images. In order to provide some coverage in the regions of the sky that would fall in the interchip gaps, the positions of successive exposures of a given field were offset by $\sim1'$ relative to each other. In general, the first exposure was at the nominal (tabulated) position, the second shifted by $41''5$ in α and $-62''3$ in δ, and the third with a shift of $-41''5$ and $62''3$ in α and δ. In a few cases an additional position with $\Delta\alpha = 20''8$ and $\Delta\beta = 31''1$ was observed. For a few fields, observations have been repeated because of bad seeing or pointing errors.

The KPNO imaging observations were made on 2000 May 4–7 and May 9 UT. A log of the observations is given in Table 3, which lists for each group of observations the date of the observations, the subfield name, the integration time and the number of exposures, and the seeing (delivered image quality expressed as FWHM in arcseconds of bright unsaturated stars) range of each exposure.

During a portion of the observing run, the pointing of the telescope was incorrectly initialized, resulting in approximately a $24'$ error in the pointing for some fields. These are noted in
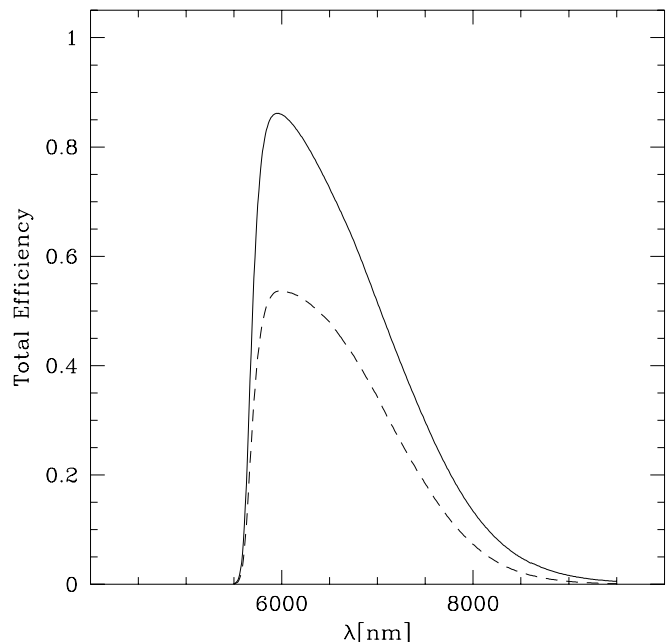

Fig. 1.—Transmission curve of the R-band filter (*solid line*) used for the observations. The dashed line indicates the combined response when also considering the CCD quantum efficiency, the throughput of the prime-focus corrector, and the atmospheric absorption with a typical air mass of 1.2.

ID	α (J2000)	δ (J2000)	No. of 10 Minute Obs.
FLS 2	17 17 48.12	+61 06 00.0	3
FLS 4	17 08 32.33	+60 32 00.0	3
FLS 5	17 13 13.17	+60 32 00.0	3
FLS 6	17 17 45.01	+60 32 00.0	3
FLS 7	17 22 25.85	+60 32 00.0	3
FLS 8	17 27 06.69	+60 32 00.0	3
FLS 9	17 05 44.94	+59 57 00.0	3
FLS 10	17 10 12.89	+59 57 00.0	5
FLS 11	17 14 48.65	+59 57 00.0	5
FLS 12	17 19 24.61	+59 57 00.0	4
FLS 13	17 23 59.47	+59 57 00.0	5
FLS 14	17 28 29.33	+59 57 00.0	3
FLS 15	17 05 56.30	+59 22 00.0	3
FLS 16	17 10 25.14	+59 22 00.0	3
FLS 17	17 14 54.99	+59 22 00.0	4
FLS 18	17 19 20.82	+59 22 00.0	4
FLS 19	17 23 53.67	+59 22 00.0	3
FLS 20	17 28 22.51	+59 22 00.0	3
FLS 22	17 10 18.66	+58 47 00.0	3
FLS 23	17 14 46.17	+58 47 00.0	3
FLS 24	17 19 12.00	+58 47 00.0	3
FLS 25	17 23 37.32	+58 47 00.0	3
FLS 26	17 28 02.83	+58 47 00.0	3
FLS 28	17 12 58.88	+58 12 30.0	3
FLS 29	17 17 19.44	+58 12 00.0	3
FLS 30	17 21 40.00	+58 12 30.0	3
ELAIS 2	16 10 01.00	+55 23 06.0	3
ELAIS 5	16 08 00.00	+54 48 06.0	5
ELAIS 6	16 12 06.76	+54 48 06.0	7
ELAIS 9	16 08 02.04	+54 13 06.2	9

NOTE.—Units of right ascension are hours, minutes, and seconds, and units of declination are degrees, arcminutes, and arcseconds.

the observing log. Since the 24′ offset did not map exactly onto our subfield grid, we chose to make stacked or combined images for several of the subfields. This was done for subfields 11 and 17 in the FLS region and subfields 6, 9, and 10 of ELAIS-N1. In Figures 2 and 3, we show the positions of each subfield on the sky with respect to the fields that have been covered with the IRAC and MIPS instruments on board *Spitzer*. In Figure 3 we display the position of the subfields in the ELAIS-N1 region and the region observed with ISOCAM as part of ELAIS. The shaded square indicates the area that has been observed to test the MIPS 24 μm confusion limits, as part of the FLS observations.

3. DATA REDUCTION

3.1. *Basic Reductions*

The processing of the raw Mosaic-1 exposures followed the steps outlined in version 7.01 of the NOAO Deep Wide-Field Survey Mosaic Data Reductions Guide[4] and discussed in Jannuzi et al. (2004). The bulk of the software used to process the images and generate combined images for each subfield from the individual 10 minute exposures is described by Valdes (2002) and contained as part of the MSCRED software package (ver. 4.7), which is part of IRAF.[5]

---

[4] See http://www.noao.edu/noao/noaodeep/ReductionOpt/frames.html.
[5] IRAF is distributed by the National Optical Astronomy Observatory, which is operated by the Association of Universities for Research in Astronomy (AURA), Inc., under cooperative agreement with the National Science Foundation.

The image quality of the final stacks is variable, as was the seeing during the run. Users of the images should be aware that the detailed shape of the point-spread function (PSF) in a given image stack could be variable across the field, not only because of residual distortions in the camera but also because a given position in the field might be the average of different input images, each with its own PSF. No attempt was made to match the PSFs of the individual images before combining the images.

In a survey area this large, there will be fields with very bright stars. This can cause some regions of the survey area to be impacted by scattered light from these stars. Some effort was made to minimize this impact during the observations (by shifting pointings) and reduction of the images (through masking of affected regions in some images to allow unaffected images to be the sole contribution to the stacked image), but users of the images should be aware that some scattered light will have made it into some of the stacks. An example of a subfield with significant scattered light is FLS 15.

Flat-fielding of the images was accomplished through the application of calibration files generated first from observations of a flat-field screen inside the dome at the 4 m and from a "supersky" flat constructed by combining the majority of the FLS and ELAIS-N1 images (with objects masked and rejected). The result is generally excellent flat-fielding of the sky (with some fields with slightly different sky color, due to moonlight or twilight). Users should be aware that there are likely to be some color-dependent variations between and within the eight CCDs, meaning that uncorrected errors in the photometry of a given object, attributable to the flat-fielding correction not being derived from a source with color matched to the color of that object, on the order of 1%–3% could still be present in the data even though the sky is generally quite "flat."

3.2. *Astrometric Calibration*

The astrometric calibration of the Mosaic-1 images is accomplished in two steps. First, the high-order distortions in the field, which will in general be common to all our exposures (those anticipated to be the result of the optics or CCD placement and, as a result, stable over the course of an observing run or season) are calibrated using observations of an astrometric standard field. These distortions can be wavelength dependent, so the calibration is made for the specific filter being used. These images are analyzed to produce a default correction for each of the CCDs. Low-order corrections (translational offset, small rotation, and scale adjustments needed to compensate for pointing errors, instrument mounting variations between runs, and atmospheric effects) are corrected on an exposure-by-exposure basis using the many catalog objects in each exposure, the previously mentioned knowledge of the high-order distortions as a function of CCD position, and the software MSCCMATCH in IRAF. The astrometric calibration has been performed using the protocol developed for the reduction of the NOAO Deep Wide-Field Survey (NDWFS) data, which assumes as astrometric reference the USNO-A2.0 catalog (Monet et al. 1998). Adopting the GSC II,[6] which became available after the development of the NDWFS reduction protocol,

---

[6] The Guide Star Catalog II is a joint project of the Space Telescope Science Institute and the Osservatorio Astronomico di Torino. STScI is operated by AURA, Inc., under NASA contract NAS 5-26555. The participation of the Osservatorio Astronomico di Torino is supported by the Italian Council for Research in Astronomy. Additional support is provided by the European Southern Observatory, the Space Telescope European Coordinating Facility, the international Gemini Project, and the European Space Agency Astrophysics Division.

TABLE 3
Log of Observations

Subfield	Exposure Time (s)	Seeing Range (arcsec)	Photometric Conditions
2000 May 4:			
FLS 4	3×600	1.4–1.5	Light cirri on sunset
FLS 5	3×600	1.4–1.45	Photometric
FLS 6	3×600	1.5–1.6	
FLS 7	3×600	1.2–1.5	
FLS 8	3×600	1.2–1.3	
FLS 10	5×600	0.98–1.15	
FLS 11	3×600	0.97–1.15	
FLS 12	4×600	0.79–1.3	
FLS 17	4×600	0.8–0.95	
2000 May 5:			
ELAIS 5	3×600	1.07–1.25	Photometric
FLS 15	3×600	1.05–1.12	
FLS 16	3×600	0.98–1.04	
FLS 20	3×600	0.88–0.9	
FLS 19	3×600	0.85–0.87	
FLS 18	4×600	0.77–0.88	
FLS 24	3×600	0.87–0.95	
FLS 23	3×600	0.9–0.94	
FLS 22	3×600	0.81–0.86	
FLS 25	3×600	0.85–0.9	
FLS 13	1×600	0.9	
2000 May 6:			
FLS 13	4×600	1.05–1.25	Light cirri
FLS 11[a]	2×600	0.95–1.1	Nonphotometric
ELAIS 6[a]	4×600	0.88–0.95	
ELAIS 9[a]	4×600	0.86–0.95	
ELAIS 10[a]	4×600	0.87–1.0	
FLS 14[a]	4×600	0.84–0.85	
2000 May 7:			
ELAIS 2	3×600	1.09–1.2	Cirri
FLS 26	3×600	1.0–1.2	Nonphotometric
FLS 28	3×600	0.96–1.0	
FLS 29	3×600	0.95–1.2	
FLS 30	3×600	1.02–1.07	
FLS 9	3×600	1.05–1.1	
FLS 2	3×600	0.94–0.98	
FLS 5	3×600	0.9–1.06	
FLS 6	3×600	0.9–0.91	
ELAIS 5	2×600	0.9–1.1	
ELAIS 6	3×600	0.9–1.1	
FLS 14	3×600	0.86–0.92	
2000 May 9:			
ELAIS 9	5×600	1.0–1.2	Nonphotometric

[a] Observed 24′ south of the originally intended position.

might improve the quality of the astrometric solutions, and this might be done if a rereduction of the data set is done in the future. As we discuss further below, the anticipated improvement would be slight. For the images described in this paper, our solutions for the mapping of the Mosaic-1 pixels into a world coordinate frame had an rms scatter of between 0″.3 and 0″.45, depending on the particular field.

After each image was provided with an improved astrometric calibration, it was tangent-plane projected with respect to the FLS and ELAIS-N1 field center positions listed above. Following projection, the individual exposures (typically three for a given region of the sky) could be combined into a final, stacked, image. These are the images currently being made available in the *Spitzer* and NOAO archives.

During the final stages of the data reduction, when the individual images were being combined to make the final image stacks, it was determined that there was an error in the high-order astrometric correction file for the Harris *R*-band filter affecting the adjacent edges of CCDs 7 and 8 in the Mosaic-1 camera. The original solutions for the high-order distortion terms were determined on a chip-by-chip basis with no requirement that the solution be continuous across the entire field. In general, while this requirement was not imposed, it was met by the solutions provided by NOAO. However, for the *R* band the solution available at the time we were reducing the data was discontinuous at the CCD 7 and CCD 8 boundary. Since our image stacks are made from the combination of three or more images that are offset by 30″ to an arcminute from each other, this difference between the solutions for the two CCDs can result in a mismapping, into right ascension and declination space, of a region of the sky imaged first on CCD 7 and then on CCD 8. The error is small
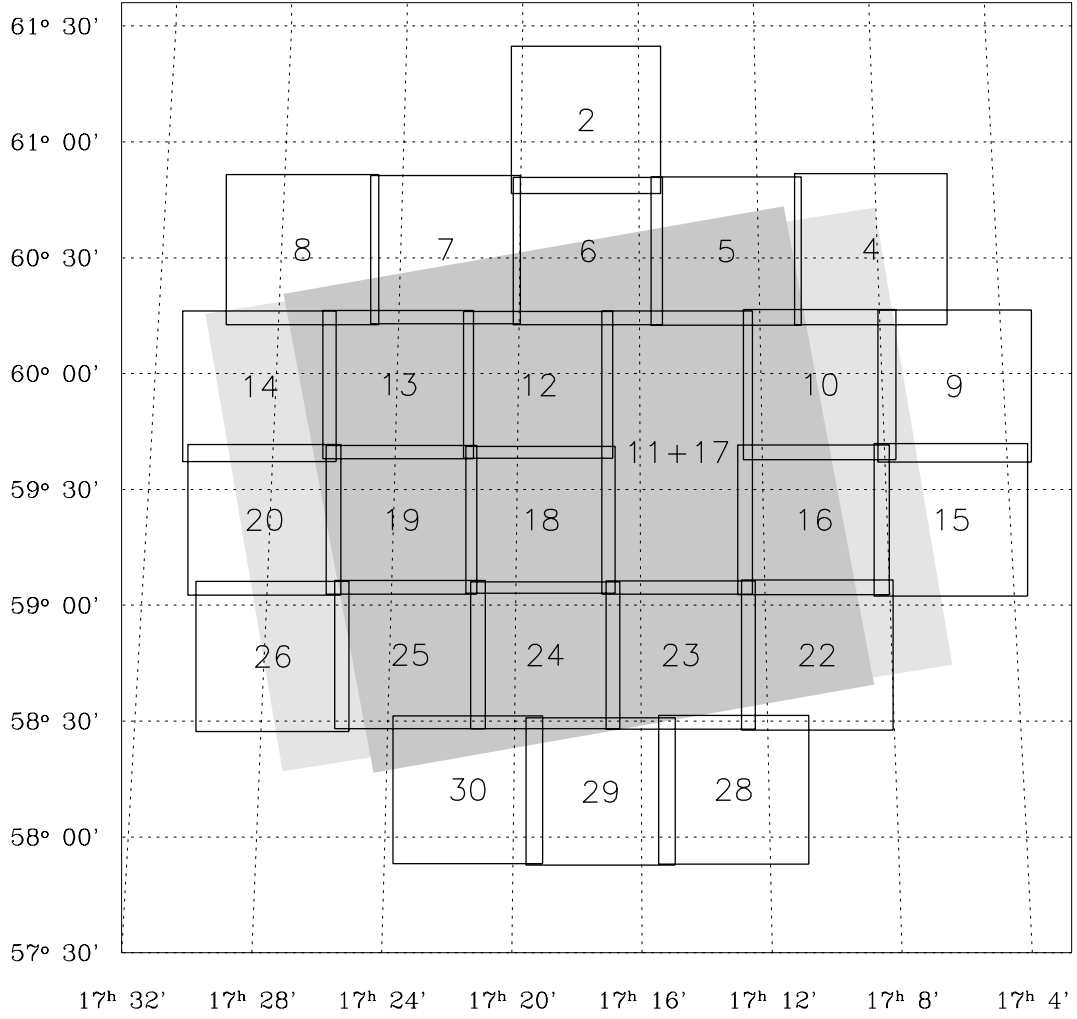
Fɪɢ. 2.—KPNO fields in the FLS region, covering most of the MIPS (*light gray*) and IRAC (*dark gray*) *Spitzer* observations.

and introduces at most an additional $0\rlap{.}''1$ uncertainty to the positions of sources in the affected region (which is located in the southeast corner of each field, about 25% of the field up from the southern edge), but it will result in a degradation of the PSF for objects affected in this region. The size of the affected region in each subfield is approximately $8\rlap{.}'5$ east-west and $2\rlap{.}'5$ north-south, or a bit less than 2% of the surveyed area.

3.3. *Photometric Calibration*

Since not all the subfields were observed during nights with photometric conditions (see Table 3), we derived a coherent photometric system in two steps. First, we computed the relative photometric zero points between the different stacked images of the subfields. Since each subfield overlaps its neighbor by approximately $2'$, we can estimate the extinction difference between them using a set of common sources. This can be expressed in terms of a zero point, which, by definition, includes the effects of air mass and extinction. Because each frame has multiple overlaps, the number of frame-to-frame magnitude differences is overdetermined with respect to the number of frames. Therefore, one can derive the relative zero point for each frame simultaneously by using a least-squares estimator. We extracted the sources from each subfield using as a first guess for the zero point that which we computed for a central subfield (No. 18 and No. 5 for the FLS and ELAIS-N1

fields, respectively). For each overlap between contiguous fields, we selected the pairs of stars with magnitude $18 < R < 21$ and computed the median of the difference in magnitudes using a 3 σ clipping procedure. The magnitudes considered were the auto magnitudes (MAG_AUTO) from SExtractor, which are fairly robust with respect to seeing variations. To estimate the relative zero points in the sense of least squares, we minimized the sum

$$\sum_{i>j} N_{ij}^2 (z_i - z_j - \Delta_{ij})^2, \qquad (1)$$

where z_i is the variation with respect to the initial guess of the zero point of subfield i and Δ_{ij} is the median of the differences of magnitude for the set of the N_{ij} source pairs in the overlapping region between subfields i and j. Solving the linear system obtained by requiring that the derivatives of this sum with respect each z_i be equal to zero, we corrected the initial guesses for the zero points. The procedure was then iterated until the number of pairs N_{ij} became stable.

The second step was to make use of those fields observed under photometric conditions in order to converge on the best zero point. Standards were measured several times over a broad range of air masses on the first two nights of the observations, which had the best photometric conditions (see Table 3). Only
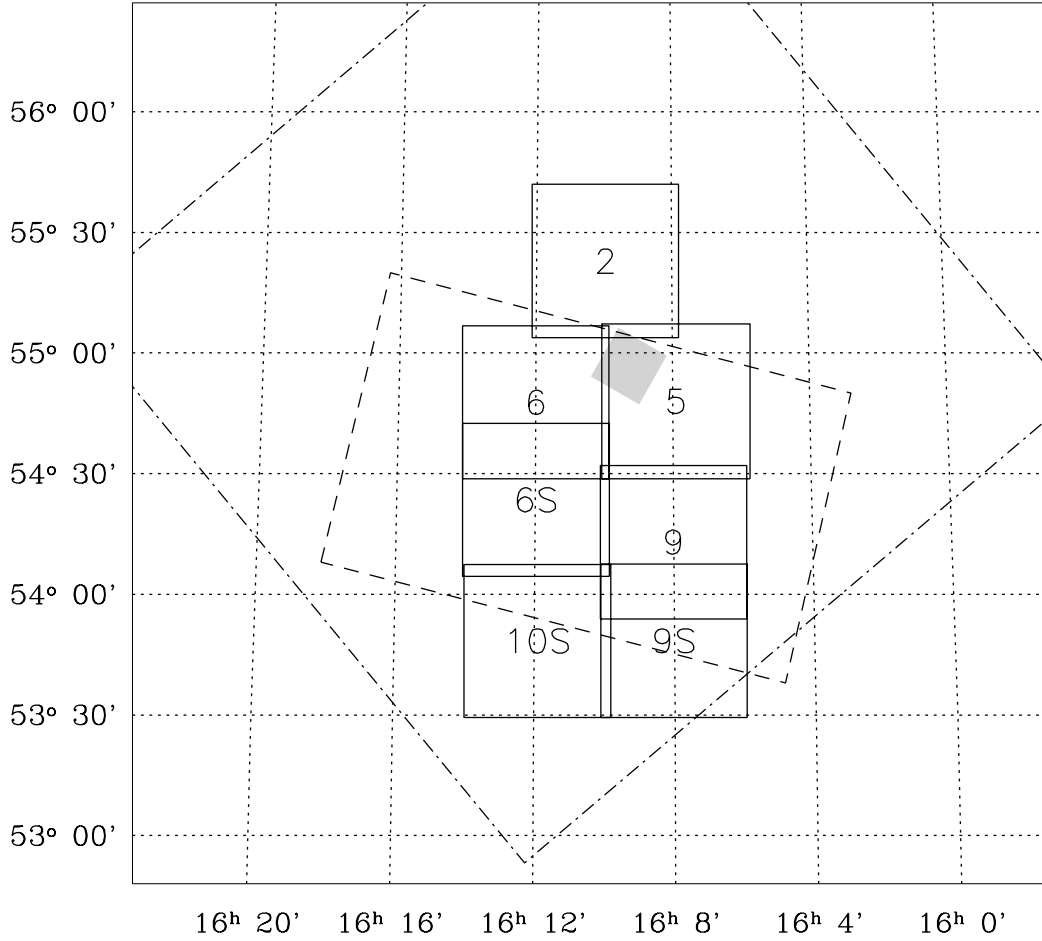
FIG. 3.—KPNO fields in the ELAIS-N1 region. The dashed line corresponds to the region observed by ISOCAM at 14.3 μm (Oliver et al. 2000). The gray shaded square is the field observed with *Spitzer* to test the MIPS 24 μm confusion limit. The SWIRE planned field (Lonsdale et al. 2003) is marked with a dash-dotted line.

the second night (May 5) was really photometric, since all the measurements are coherent (see Fig. 4). Magnitudes were calibrated to the Kron-Cousins system using standards taken from Landolt (1992). They have been obtained using an aperture of 6″ in diameter, large enough to obtain accurate measurements according to the growth curves of all the measured stars. We have fitted the linear relationship

$$m = m_0 - 2.5 \log{(C/t_{\exp})} + m_X A \qquad (2)$$

with m magnitude of the Landolt standard, A air mass during the observation, C counts during the exposure time $t_{\exp}$, and m_0 and m_X the zero-point and extinction terms, respectively. We used an iterative 3 σ clipping to discard deviant measurements, finding the best fit for $m_0 = 25.42$ and $m_X = -0.09$. The standard deviation of the residuals for the best fit is 0.03.

4. DATA PRODUCTS

The analysis of the survey data produced a set of intermediate and final products, images and catalogs, which are publicly available at the *Spitzer* Science Center and NOAO Science Archive.[7] In particular, we provide the astronomical community with the following.
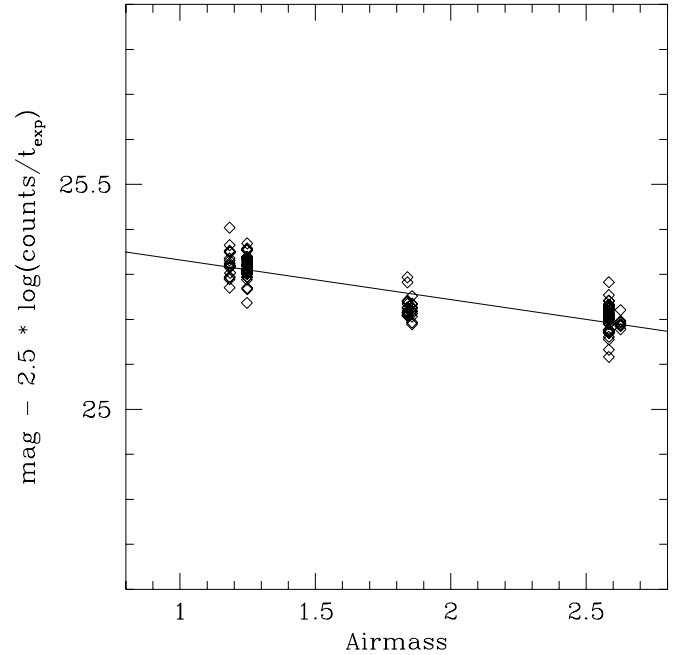
FIG. 4.—Dependence of zero point on air mass. Each diamond is a standard star used in the calibration with nine standard fields observed during the night of 2000 May 5.

Co-added (stacked) images of the subfields.—Sky-subtracted, fully processed co-added frames for each subfield. The sub-fields are mapped using a tangential projection. The size of each FITS image is 320 Mbyte. For each image, a bad-pixel mask and an exposure map are given (in the pixel-list IRAF format). The photometric zero point of each subfield after the absolute photometric calibration of the frame appears in the header of the image. A full description of the header keywords is available at the archive sites.

Low-resolution field images.—Sky-subtracted, fully pro-cessed co-added images of the whole field. The images have been created to give a general overview of the FLS and ELAIS-N1 fields and were produced using a $1.''3$ pixel size (corresponding to 5 times the original size of the pixel). Users are discouraged from using them to extract sources and compute photometry. These images have sizes of approxi-mately 380 and 80 Mbyte.

Single-subfield catalogs.—Object catalogs associated with each subfield. A full description of the parameters available is given in the following section. The catalogs are in ASCII format.

5. CATALOGS

The main goal of this survey is to catalog galaxies and faint stars and make a first distinction between stars and galaxies on the basis of their intensity profiles. Several bright objects (mainly stars) are saturated and excluded from the catalog, but they can be found in catalogs from shallower surveys (such as SDSS in the case of the FLS region; see, e.g., Stoughton et al. 2002; Hogg et al. 2004). The source extraction was performed with the SExtractor package (Bertin & Arnouts 1996; ver. 2.3), which is well suited for surveys with low-to-moderate source density as is the case for our surveys.

5.1. *Detection*

Several parameters have to be fixed to achieve an efficient source extraction with SExtractor. The first problem is the evaluation of the background. SExtractor proceeds by com-puting a *minibackground* on a scale large enough to contain several faint objects and filtering it with a boxcar to avoid contamination by isolated, extended objects. Finally, a full-resolution background map is obtained by interpolation and is subtracted from the science image. In our case, many bright stars populate the FLS field, since it is at a moderate Galactic latitude ($34.°9$), while the problem is less important in the case of the ELAIS-N1 field (latitude $44.°9$). To evaluate a back-ground that is not locally dominated by bright stars, we adopted meshes of 128×128 pixels for the minibackground corresponding to $33.''0$ and used a 9×9 boxcar for the median filtering.

In order to improve the detection of faint sources, the image is filtered to enhance the spatial frequency typical of the sources with respect to that of the background noise. A Gaussian filter with a FWHM similar to the seeing of the image (in our case 4 pixels, since the overall seeing is $1.''1$) has been used. Although the choice of a convolution kernel with a constant FWHM may not always be optimal, since the seeing varies in the different images, the impact on detectability is fairly small (Irwin 1985). Moreover, it has the advantage of requiring no changes in the relative detection threshold.

Finally, the detection is performed on the background-subtracted and filtered image, looking for groups of connected pixels above the detection threshold. Thresholding is in fact the most efficient way to detect low surface brightness objects. In our case, we fixed the minimum number of connected pixels to 15 and the detection threshold to 0.8 (in units of the standard deviation of the background noise), which corre-spond to a typical limiting surface brightness $\mu_R \sim 26$ mag arcsec^{-2}. For the detection, we also made use of the exposure map as a weight considered to set the noise level for each pixel. Some pixels have a null weight because they correspond to saturated objects, trails of bright objects, and other artifacts. These pixels are also marked in the bad-pixel mask, and the false detections around these image artifacts are flagged and easily excluded from our final catalogs. Only objects detected with a signal-to-noise ratio greater than 3 (based on the total magnitude errors) are accepted in our final catalog.

Although not well suited to detecting objects in crowded fields, SExtractor also allows one to deblend close objects using a multiple isophotal analysis technique. Two parameters affect the deblending: the number of thresholds used to split a set of connected pixels according to their luminosity peaks, and the minimal contrast (light in a peak divided by the total light in the object) used to decide whether to deblend a sub-object from the rest of the object. In our analysis we used a high number of thresholds (64) and a very low minimal contrast ($1.5 \ e^{-5}$). Nevertheless, a few blended objects still remain in the catalogs. Visual inspection or other extraction algorithms that are more efficient in crowded fields (e.g., DAOPHOT) are needed to treat these particular cases.

5.2. *Photometry*

The photometry has been performed on the stacked images. Several measurements were made: aperture and isophotal magnitudes, and an estimate of the total magnitudes. We mea-sured the aperture magnitude within a diameter of $3''$, roughly corresponding to 3 times the overall seeing. Total magnitudes (MAG_AUTO) are estimated using an elliptical aperture with an approach similar to that proposed by Kron (1980). Since these fields have been selected in sky regions with low Galactic extinction in order to observe extragalactic infrared sources, the corrections for Galactic extinction (Schlegel et al. 1998) are small: 0.06 and 0.01 on average for the FLS and ELAIS-N1 fields, respectively.

The total magnitudes of sources close to bright objects are usually inaccurate, since the local background is affected by the halo of the bright objects and the Kron radius is not cor-rectly computed. To improve the photometry for these sources, we have subtracted bright saturated stars from the images and excluded from the catalogs the sources detected in square boxes around these stars where the subtraction is not correct. Moreover, we have considered bright extended galaxies and excluded from the catalogs all the sources inside the Kron ellipses of the galaxies. In fact, most of these sources are bright regions of the galaxies or their photometry is highly affected by the diffuse luminosity of the galaxies.

To subtract bright saturated stars from the images, we have computed radial density profiles on concentric annuli around the stars. Then, after subtracting these profiles, we removed the diffraction spikes by fitting their profiles along the radius at different angles with Chebyshev polynomials. As is visible in Figures 5 and 6, the background is much more uniform and the spikes become shorter. This improves the photometry for the objects surrounding the stars and avoids the detection of faint false sources on the diffraction spikes.

The correction works well for most of the stars, although we exclude the immediate neighborhood from the catalogs. In the
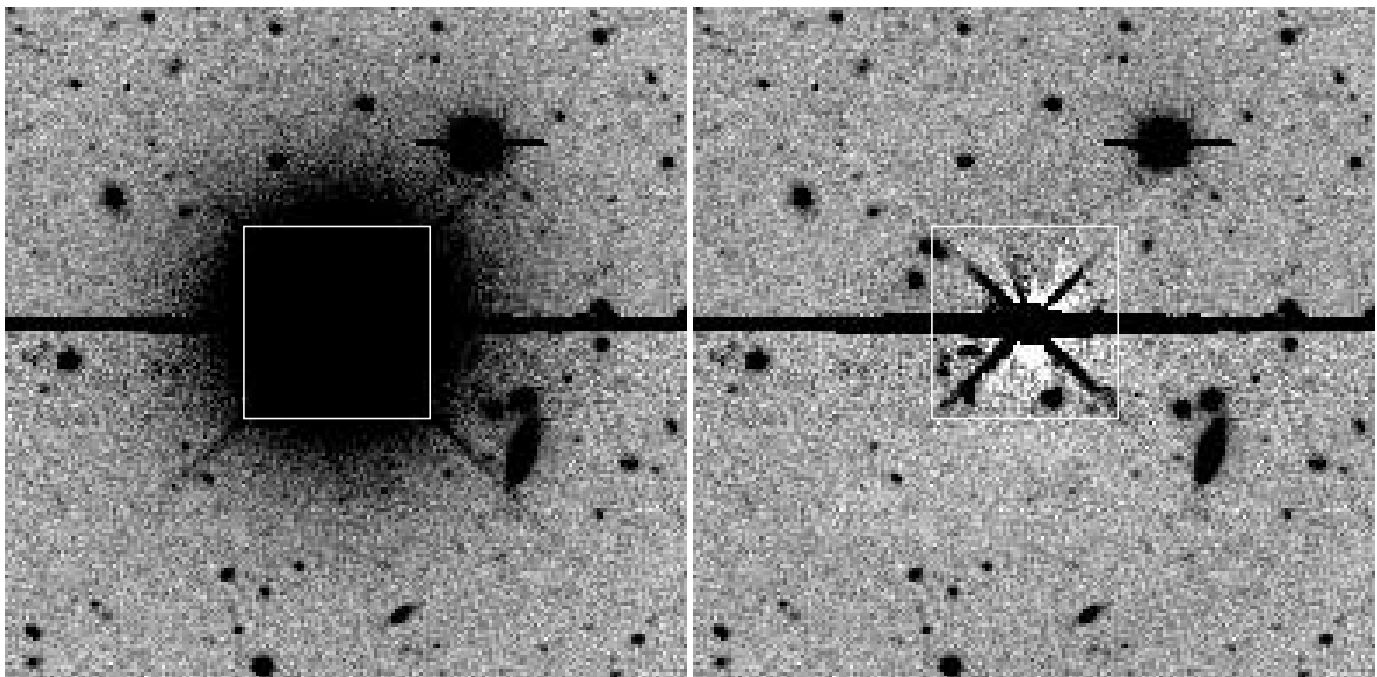
FIG. 5.—A $1'.5 \times 1'.5$ field around a bright saturated star in field FLS 6 before and after the star removal. The overplotted square delimits the region that is not considered in the final catalog.

case of very bright stars (see Fig. 6), multiple reflections between the CCD and the optics make the subtraction of a median radial profile difficult, and a faint halo is still visible after the correction.

5.3. *Star-Galaxy Separation*

SExtractor uses a neural network to separate starlike from extended sources, returning a stellarity index (CLASS_STAR) with values between 1 (a perfect starlike object) and 0. The distribution of this index as a function of the magnitude in one of our fields (FLS 18) is shown in Figure 7.

The standard neural network of SExtractor has been trained for FWHM seeing values between $0''.02$ and $5''.5$ and for images that have $1.5 < \mathrm{FWHM} < 5$ pixels. It is therefore perfectly suited to our images.

Although at bright magnitudes two sequences can easily be distinguished (see Fig. 7), for fainter magnitudes it becomes more difficult to separate extended from point objects. In order
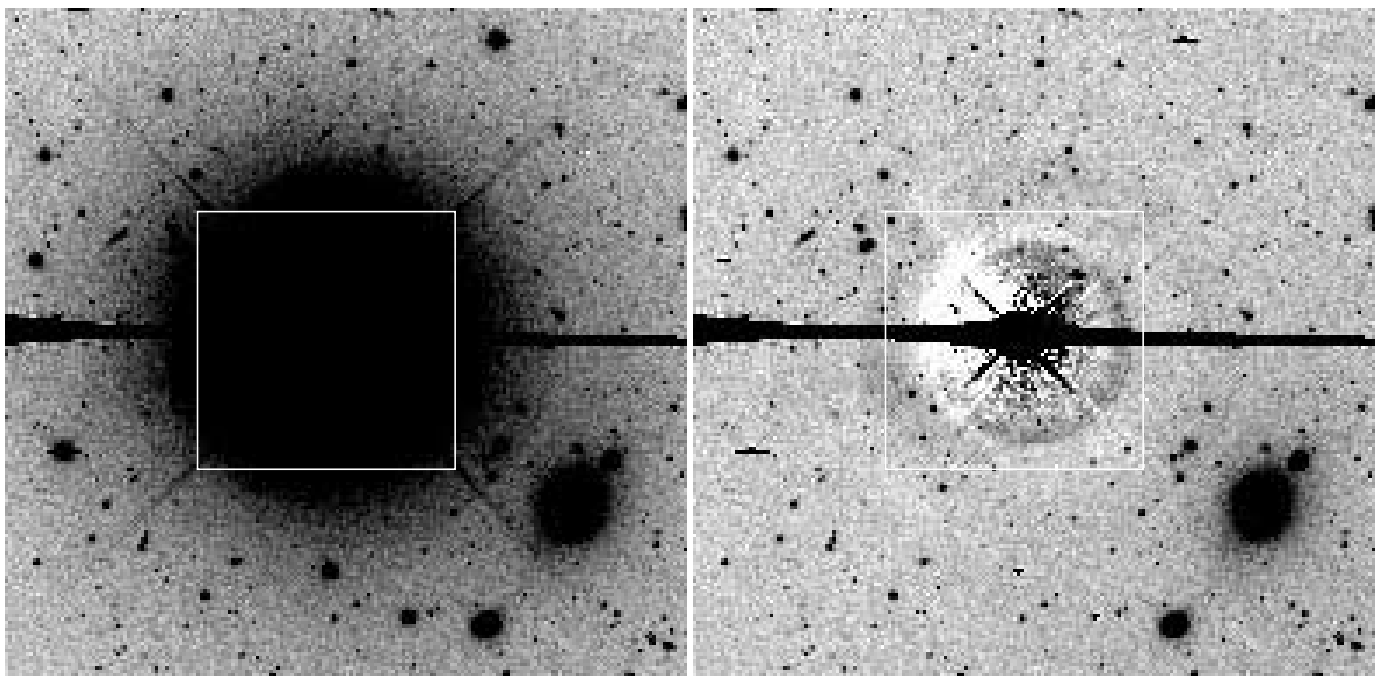

FIG. 6.—A $7' \times 7'$ field around a bright saturated star in field FLS 13 before and after the star removal. The overplotted square delimits the region that is not considered in the final catalog. Multiple reflections of the star between the optics and the CCD are visible.
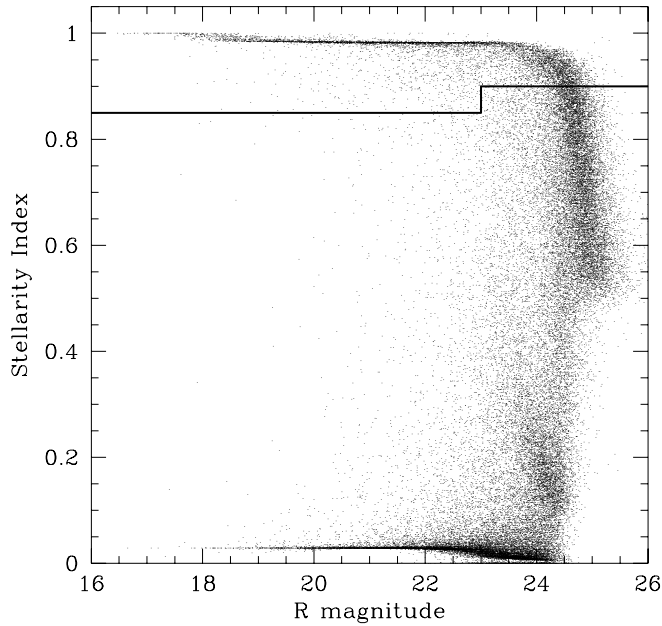
FIG. 7.—SExtractor stellarity index vs. *R* magnitude for the objects detected in field FLS 18. The solid line indicates the threshold of the stellarity index as a function of the magnitude chosen to separate stars from galaxies in our survey.

to select stars in an efficient way, we followed the technique of Groenewegen et al. (2002), choosing a threshold that is a function of the magnitude. We consider an object to be a star if

$$\text{CLASS\_STAR} > 0.85 \quad \text{for } R < 23, \tag{3}$$

$$\text{CLASS\_STAR} > 0.90 \quad \text{otherwise.} \tag{4}$$

A drawback of this technique is that at faint magnitudes, QSOs are also classified as stars. However, using multiband catalogs one can address the issue of separating stars and QSOs on the basis of their spectral energy distributions.

5.4. *Source Lists*

As an illustration, a tabulation of the first 30 entries in the FLS 2 source catalog is presented in Table 4. All magnitudes are given in the Vega system. The table lists the following.

Column (1): The full IAU designation of the source.
Columns (2)–(3): Right ascension and declination (J2000).
Columns (4)–(7): Aperture (3″ diameter) and total magnitudes and respective errors. The total magnitude corresponds to the MAG_AUTO magnitude measured by SExtractor. The magnitudes have been not corrected for Galactic extinction. The errors are those estimated by SExtractor and include only the shot noise of the measured source and background counts. Only objects detected with signal-to-noise ratio $S/N \geq 3$ (based on the total magnitude errors) and without saturated pixels are included.

Column (8): An estimate of the S/N of the detection, from the errors estimated for the total magnitude.

TABLE 4
First 30 Entries of the FLS 2 Source List

| Identification (1)	α (J2000) (2)	δ (J2000) (3)	m_{aper} (4)	ϵ (5)	m_{tot} (6)	ϵ (7)	S/N (8)	Class. (9)	Ext. (10)
FLS_R_J171814.3+604643	17 18 14.303	+60 46 43.93	21.44	0.02	21.44	0.03	38.8	0.997	0.071
FLS_R_J171804.5+604644	17 18 04.511	+60 46 44.00	23.60	0.12	23.66	0.12	8.8	0.753	0.071
FLS_R_J171847.4+604644	17 18 47.496	+60 46 44.22	24.12	0.20	24.19	0.21	5.2	0.735	0.073
FLS_R_J171822.5+604644	17 18 22.536	+60 46 44.07	22.99	0.07	22.95	0.09	12.2	0.975	0.071
FLS_R_J171840.3+604644	17 18 40.368	+60 46 44.40	23.61	0.12	23.60	0.12	9.1	0.936	0.072
FLS_R_J171729.6+604645	17 17 29.639	+60 46 45.47	24.08	0.19	23.53	0.18	6.0	0.784	0.069
FLS_R_J171739.6+604645	17 17 39.672	+60 46 45.69	24.65	0.32	24.36	0.17	6.4	0.802	0.070
FLS_R_J171808.7+604643	17 18 08.784	+60 46 43.96	20.72	0.01	20.69	0.01	104.4	0.983	0.071
FLS_R_J171824.5+604644	17 18 24.575	+60 46 44.11	20.84	0.01	20.73	0.02	67.4	0.983	0.071
FLS_R_J171817.5+604644	17 18 17.567	+60 46 44.65	22.51	0.04	22.49	0.06	18.8	0.960	0.071
FLS_R_J171851.9+604644	17 18 51.984	+60 46 44.61	20.75	0.01	20.71	0.01	94.4	0.984	0.073
FLS_R_J171914.2+604645	17 19 14.232	+60 46 45.44	22.62	0.05	22.58	0.06	18.3	0.973	0.074
FLS_R_J171734.8+604646	17 17 34.872	+60 46 46.05	23.22	0.09	23.12	0.09	12.0	0.851	0.070
FLS_R_J171912.1+604647	17 19 12.191	+60 46 47.13	24.28	0.23	24.29	0.23	4.7	0.652	0.074
FLS_R_J171841.0+604646	17 18 41.087	+60 46 46.91	23.66	0.13	23.64	0.13	8.6	0.944	0.072
FLS_R_J171747.7+604648	17 17 47.712	+60 46 48.53	24.61	0.31	24.45	0.18	6.1	0.758	0.070
FLS_R_J171726.8+604646	17 17 26.807	+60 46 46.12	23.29	0.09	22.58	0.11	10.3	0.851	0.069
FLS_R_J171827.8+604646	17 18 27.887	+60 46 46.99	23.30	0.09	22.86	0.11	9.6	0.873	0.072
FLS_R_J171834.5+604648	17 18 34.560	+60 46 48.28	23.94	0.17	23.89	0.14	7.6	0.945	0.072
FLS_R_J171838.2+604644	17 18 38.279	+60 46 44.40	20.22	0.01	20.19	0.01	155.1	0.985	0.072
FLS_R_J171631.4+604647	17 16 31.487	+60 46 47.20	23.47	0.11	21.60	0.06	18.8	0.947	0.064
FLS_R_J171731.9+604646	17 17 31.967	+60 46 46.99	23.09	0.08	22.29	0.09	11.6	0.749	0.069
FLS_R_J171821.9+604645	17 18 21.911	+60 46 45.91	23.17	0.08	22.98	0.11	9.6	0.434	0.071
FLS_R_J171719.7+604649	17 17 19.704	+60 46 49.00	23.81	0.15	23.74	0.21	5.1	0.928	0.068
FLS_R_J171618.3+604647	17 16 18.312	+60 46 47.63	24.48	0.27	24.22	0.18	6.0	0.671	0.063
FLS_R_J171843.1+604648	17 18 43.128	+60 46 48.39	23.74	0.14	23.84	0.14	7.6	0.955	0.073
FLS_R_J171733.5+604649	17 17 33.503	+60 46 49.40	23.62	0.12	23.33	0.16	6.7	0.974	0.069
FLS_R_J171730.6+604649	17 17 30.671	+60 46 49.58	24.10	0.19	23.08	0.14	7.8	0.879	0.069
FLS_R_J171851.1+604645	17 18 51.143	+60 46 45.26	19.53	0.00	19.49	0.00	258.5	0.985	0.073
FLS_R_J171646.7+604647	17 16 46.751	+60 46 47.28	22.53	0.05	22.05	0.07	16.4	0.043	0.065
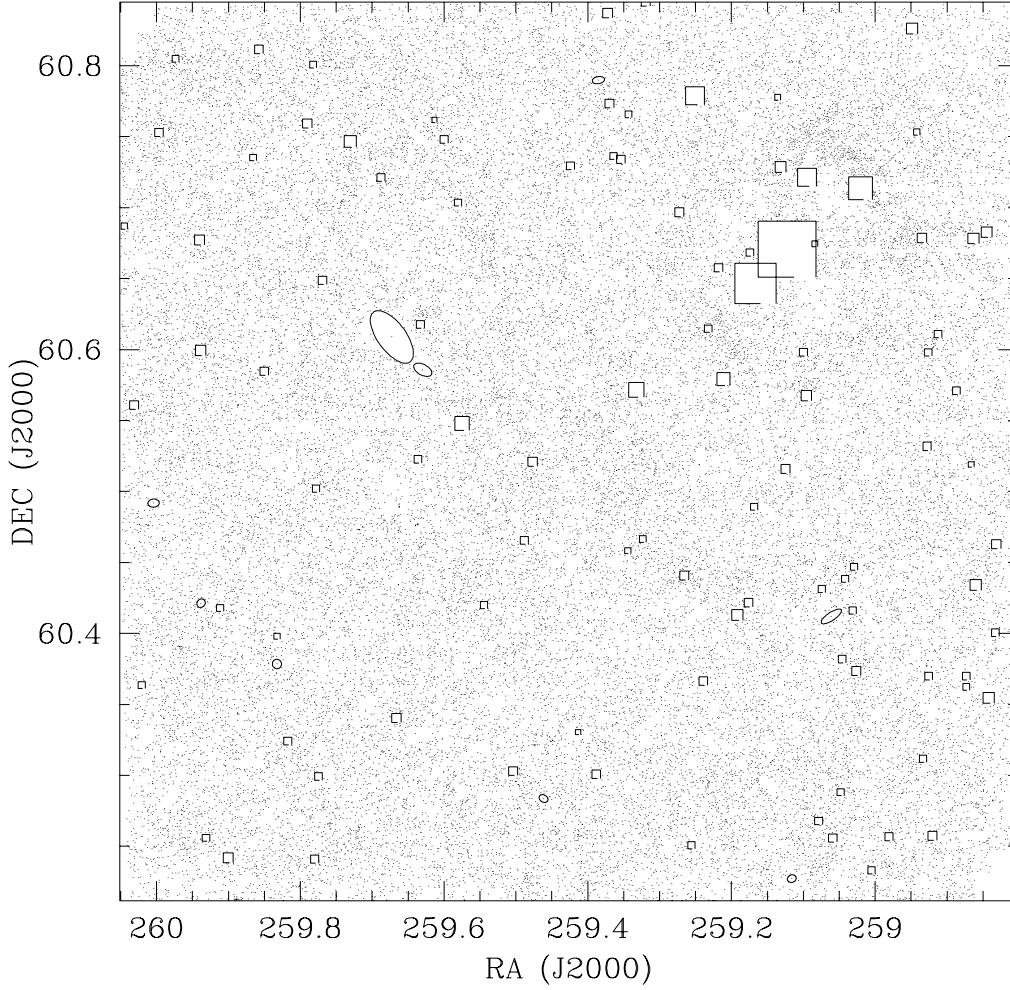
Fig. 8.—Projected distribution of galaxies extracted from the FLS 6 image. Square masks around the bright saturated stars and elliptical masks around bright extended galaxies in the field are shown.

Column (9): The stellarity index computed by SExtractor.

Column (10): The Galactic extinction, taken from Schlegel et al. (1998). As an example, we show in Figure 8 the projected distribution of the galaxies detected in the FLS_6 field.

All the catalogs in the archive are in ASCII format. Each catalog has been verified with several tests to check the reliability of the measured quantities with other sets of data. The results of some of these tests are described in the next section.

6. SURVEY PERFORMANCE

The characteristics of the data obtained by the present survey are summarized in Table 5, which lists in column (1) the name of the subfield, in columns (2)–(3) the center of the subfield, in column (4) the seeing of the combined image, in columns (5)–(6) the 3 σ and 5 σ limiting Cousins R magnitudes, and in columns (7)–(8) the number of galaxies and stars with S/N $\geq$ 3 that are not saturated.

We measured the limiting R Cousins magnitude inside the aperture with the highest signal-to-noise ratio in the case of a Gaussian PSF dominated by the sky. Considering a Gaussian profile, the S/N inside an aperture R can be written as

$$ S/N = \frac{\int_0^R C e^{-2 \ln (2r/W)} \, dr}{\sqrt{\pi(R^2/\Delta^2)\sigma_S^2}} \qquad (5) $$

with W the FWHM, C the central intensity of the source, Δ the pixel size, and σ_S the sky noise. The R for which S/N is maximal corresponds to the R for which $\partial(S/N)/\partial R = 0$. This condition is realized at $R \approx 1.35W/2$, that is, an aperture of 1.35 FHWM. Since we are considering in our catalogs an aperture of 3″ and our typical FHWM is 1″0, these values are slightly deeper than what one can find in our catalogs.

The fraction of spurious objects was estimated by creating catalogs from the survey images multiplied by −1. Since ideally the noise is symmetric, we can use these images to produce a catalog of spurious sources by applying the same criteria of extraction that have been used with the real images. Analyzing the central square degree, false positive detections occur only at faint magnitudes ($R > 23.8$). Considering all the 3 σ objects, in the magnitude interval $23.5 < R < 24.5$ there are 150 false positive detections per square degree, corresponding to 0.5% of the total number of sources. In the magnitude interval $24.5 < R < 25.5$ there are 119 false positive detections per square degree, which corresponds to 17% of the total of number of sources detected in this magnitude range.

6.1. Astrometry

To assess the accuracy of the astrometric calibration, we compared the positions of the stars inside the FLS field with those available from the Sloan survey (Data Release 1;

TABLE 5
PROPERTIES OF IMAGES AND EXTRACTED CATALOGS

ID (1)	α (J2000) (2)	δ (J2000) (3)	Seeing (arcsec) (4)	$m_{\lim}(5\,\sigma)$ (mag) (5)	$m_{\lim}(3\,\sigma)$ (mag) (6)	N_{gals} (7)	N_{stars} (8)
FLS 2	17 17 45.70	61 05 44.12	1.08	25.59	26.15	34,766	6787
FLS 4	17 08 27.23	60 32 10.74	1.57	24.72	25.28	18,016	2962
FLS 5	17 13 10.74	60 31 44.01	1.06	25.64	26.20	36,372	5012
FLS 6	17 17 42.13	60 31 42.33	1.02	25.78	26.34	36,988	5050
FLS 7	17 22 21.27	60 32 06.70	1.54	24.86	25.42	19,959	1316
FLS 8	17 27 02.18	60 32 07.10	1.36	25.09	25.64	22,392	3049
FLS 9	17 05 42.63	59 56 46.44	1.14	25.58	26.13	34,985	5254
FLS 10	17 10 07.30	59 57 07.22	1.24	25.63	26.19	32,253	3309
FLS 11 + 17........	17 14 47.10	59 39 33.96	1.04	25.86	26.41	72,709	6865
FLS 12	17 19 19.96	59 57 03.33	1.00	25.86	26.42	35,905	4352
FLS 13	17 23 54.12	59 57 09.50	1.16	25.41	25.96	30,797	5496
FLS 14	17 28 26.67	59 56 39.57	0.98	25.51	26.06	34,672	5114
FLS 15	17 05 50.01	59 22 06.83	1.22	25.14	25.69	25,218	4450
FLS 16	17 10 19.12	59 22 07.62	1.17	25.25	25.80	26,996	4313
FLS 18	17 19 14.84	59 22 07.54	0.92	25.91	26.46	37,922	4228
FLS 19	17 23 48.01	59 22 07.27	0.97	25.64	26.19	34,771	4409
FLS 20	17 28 17.04	59 22 08.13	1.00	25.59	26.15	35,297	4278
FLS 22	17 10 12.41	58 47 07.63	0.94	25.77	26.33	35,201	4259
FLS 23	17 14 40.18	58 47 07.50	1.06	25.67	26.22	34,624	4313
FLS 24	17 19 06.04	58 47 04.74	1.03	25.71	26.26	31,151	4277
FLS 25	17 23 30.85	58 47 10.81	0.99	25.76	26.31	33,847	4682
FLS 26	17 28 00.70	58 46 43.81	1.22	25.21	25.77	22,636	5538
FLS 28	17 12 56.31	58 12 15.54	1.12	25.37	25.93	30,609	5830
FLS 29	17 17 16.96	58 11 44.23	1.12	25.52	26.07	34,524	6264
FLS 30	17 21 37.91	58 12 14.09	1.20	25.49	26.05	38,493	10099
ELAIS 2	16 09 58.00	55 22 51.47	1.20	25.18	25.74	26,960	3802
ELAIS 5	16 07 55.71	54 47 58.39	1.22	25.59	26.14	33,876	3240
ELAIS 6	16 11 59.38	54 47 43.34	1.11	25.49	26.05	34,736	3406
ELAIS 6S............	16 11 58.89	54 23 29.02	0.98	25.82	26.38	41,506	3160
ELAIS 9	16 07 59.66	54 12 59.29	1.11	25.77	26.32	38,231	2926
ELAIS 9S............	16 07 58.67	53 48 27.43	1.01	25.78	26.33	38,167	3538
ELAIS 10S..........	16 11 56.45	53 48 23.99	1.02	25.72	26.28	36,497	3496

Abazajian et al. 2003) and with radio sources from the VLA survey in the FLS field (Condon et al. 2003).

In the comparison with the Sloan sources, we considered only good objects (according to the flags) classified as stars in the Sloan catalog with R magnitude between 18 and 21. Table 6 reports the number of stars used in the comparison and the offsets between our and the Sloan positions. Typical offsets are $0\rlap{.}''1$ in right ascension and declination, with an rms of $0\rlap{.}''1$. The offsets between our catalog and the Sloan stars in the case of field FLS 18 are shown in Figure 9. The comparison with the VLA sources has been made considering all the optical counterparts down to $R = 24$ of nonextended radio sources. The offsets from the VLA positions are also on the order of $0\rlap{.}''1$.

The systematic offset between our and Sloan positions comes from the fact that our astrometry is based on the USNO-A2 catalog, while Sloan takes Tycho-2 stars as reference. Comparing the Sloan and USNO-A2 positions in the whole FLS field, we have an offset of $\Delta\alpha = 0\rlap{.}''13 \pm 0\rlap{.}''28$ and $\Delta\delta = 0\rlap{.}''15 \pm 0\rlap{.}''34$, which is in complete agreement with the offsets found in Table 6.

Finally, we compared our R-band catalog with the GSC II, finding an offset of $\Delta\alpha = -0\rlap{.}''05 \pm 0\rlap{.}''18$ and $\Delta\delta = 0\rlap{.}''22 \pm 0\rlap{.}''15$. While not large, this offset should be noted when making comparison with data sets that used the GSC II for reference.

Nevertheless, the remarkably small rms in both directions obtained comparing our and the Sloan positions suggests an intrinsic accuracy of $\lesssim 0\rlap{.}''1$ for each catalog, which is well within the requirements for slit/fiber positioning, an essential requirement for public surveys.

6.2. Photometry

The Sloan survey also allows us to compare the photometric calibration. Although the magnitude system used in that survey is different from ours, we can obtain a relationship between the R Cousins magnitude and the Sloan magnitudes using the 92 Landolt stars that have been observed by the Sloan group to calibrate their observations (Smith et al. 2002). Before making the comparison, we converted the r' and i' magnitudes to the SDSS 2.5 m natural system, using the equations

$$r_{\mathrm{SDSS}} = r' + 0.035(r' - i' - 0.21), \qquad (6)$$
$$i_{\mathrm{SDSS}} = i' + 0.041(r' - i' - 0.21), \qquad (7)$$

as explained at the Sloan Web site.[8] Then we obtained a relationship between R and the Sloan colors with a least-squares fit:

$$R = -0.16 + r_{\mathrm{SDSS}} - 0.26(r_{\mathrm{SDSS}} - i_{\mathrm{SDSS}}). \qquad (8)$$

Using a biweight estimator, the difference between the real R and the value estimated with equation (8) is an average of

---

[8] See http://www.sdss.org/DR1/algorithms/jeg_photometric_eq_dr1.html.

TABLE 6
ASTROMETRY AND PHOTOMETRY: COMPARISON WITH SDSS AND VLA

ID	Stars	$\langle R_{\text{Sloan}} - R \rangle$ (mag)	$\alpha - \alpha_{\text{Sloan}}$ (arcsec)	$\delta - \delta_{\text{Sloan}}$ (arcsec)	VLA Sources	$\alpha - \alpha_{\text{VLA}}$ (arcsec)	$\delta - \delta_{\text{VLA}}$ (arcsec)
FLS 2	2004	-0.050 ± 0.086	0.12 ± 0.12	0.07 ± 0.09	23	0.11 ± 0.44	0.04 ± 0.38
FLS 4	1523	0.100 ± 0.090	0.19 ± 0.12	-0.01 ± 0.10	...	...	...
FLS 5	1523	-0.054 ± 0.076	0.12 ± 0.12	0.07 ± 0.09	84	0.09 ± 0.34	0.24 ± 0.35
FLS 6	1967	-0.052 ± 0.084	0.17 ± 0.13	0.15 ± 0.10	117	0.17 ± 0.37	0.28 ± 0.36
FLS 7	1501	0.068 ± 0.101	0.11 ± 0.13	0.11 ± 0.10	76	0.10 ± 0.39	0.18 ± 0.31
FLS 8	1571	0.019 ± 0.088	0.14 ± 0.13	0.18 ± 0.09	...	...	...
FLS 9	1319	-0.053 ± 0.076	0.21 ± 0.11	0.03 ± 0.09	...	...	...
FLS 10	1509	0.007 ± 0.079	0.16 ± 0.13	0.09 ± 0.09	125	0.11 ± 0.33	0.09 ± 0.39
FLS 11 + 17	2810	-0.021 ± 0.079	0.12 ± 0.14	0.13 ± 0.08	269	0.15 ± 0.35	0.08 ± 0.38
FLS 12	2132	-0.041 ± 0.079	0.12 ± 0.12	0.18 ± 0.08	121	0.27 ± 0.32	0.22 ± 0.29
FLS 13	1412	0.093 ± 0.093	0.09 ± 0.14	0.15 ± 0.10	128	0.08 ± 0.37	0.12 ± 0.37
FLS 14	1590	-0.011 ± 0.078	0.08 ± 0.13	0.10 ± 0.09	29	0.07 ± 0.35	0.13 ± 0.47
FLS 15	1335	0.047 ± 0.087	0.22 ± 0.12	0.07 ± 0.11	...	...	...
FLS 16	1379	0.032 ± 0.080	0.18 ± 0.14	0.09 ± 0.09	106	0.21 ± 0.40	0.12 ± 0.35
FLS 18	2294	-0.008 ± 0.085	0.12 ± 0.13	0.09 ± 0.10	144	0.21 ± 0.32	0.12 ± 0.30
FLS 19	1614	-0.000 ± 0.087	0.11 ± 0.12	0.14 ± 0.09	142	0.19 ± 0.37	0.11 ± 0.37
FLS 20	1608	-0.001 ± 0.084	0.06 ± 0.13	0.11 ± 0.10	58	0.02 ± 0.31	0.14 ± 0.40
FLS 22	1461	-0.015 ± 0.079	0.17 ± 0.13	-0.11 ± 0.10	61	0.30 ± 0.35	-0.02 ± 0.35
FLS 23	1510	0.002 ± 0.081	0.10 ± 0.15	0.03 ± 0.09	121	0.09 ± 0.35	0.07 ± 0.37
FLS 24	2044	-0.025 ± 0.079	0.03 ± 0.13	0.07 ± 0.12	143	0.05 ± 0.38	0.07 ± 0.37
FLS 25	2022	-0.034 ± 0.082	0.04 ± 0.12	0.05 ± 0.09	117	0.13 ± 0.38	0.08 ± 0.36
FLS 26	1539	-0.038 ± 0.080	0.05 ± 0.13	0.00 ± 0.09	34	0.04 ± 0.40	0.17 ± 0.40
FLS 28	1273	-0.027 ± 0.078	-0.11 ± 0.16	0.05 ± 0.16	...	...	...
FLS 29	1769	-0.053 ± 0.082	-0.01 ± 0.14	0.22 ± 0.08	57	0.02 ± 0.41	0.18 ± 0.35
FLS 30	3198	-0.072 ± 0.082	0.02 ± 0.13	0.17 ± 0.11	23	0.09 ± 0.40	0.25 ± 0.30
Average	...	-0.007 ± 0.016	0.10 ± 0.03	0.09 ± 0.02	...	0.12 ± 0.08	0.13 ± 0.08

0.0001 (with an rms of 0.007). Despite the large scatter, the relationship is useful from a statistical point of view, since we are interested only in confirming our magnitude zero point.

We have therefore compared the magnitudes of the stars in the FLS fields with the values deduced from the Sloan survey with equation (8). Table 6 summarizes the median differences
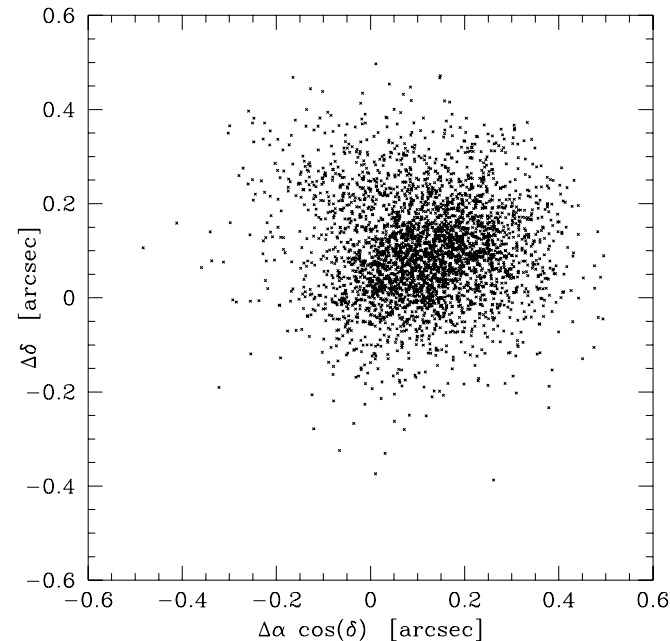

FIG. 9.—Comparison between the positions of stars in common with the Sloan survey for field FLS 18. Offsets are computed as our minus Sloan positions.

in magnitude between our measurements (auto magnitudes) and the *model* complete magnitude as computed by Sloan for stars with magnitude $18 < R < 21$ in the different FLS fields. In Figure 10 we show the distribution of the magnitude offsets in the case of the central field, FLS 18, while in Figure 11 we illustrate the offsets for the various fields. Our calibration agrees on average with the Sloan one, since the average difference between our and the Sloan measurements is -0.007 ± 0.016. The biggest differences are found in the external subfields, where the relative zero is not well constrained because of the low number of stars in common between adjacent subfields (see Fig. 11).

6.3. Number Counts

Counting galaxies and stars as a function of the magnitude allows one to evaluate the overall characteristics of a catalog such as depth and homogeneity. In Figures 12 and 14, we show star and galaxy counts in the FLS region and compare them with analogous counts using the Sloan Digital Sky Survey (Stoughton et al. 2002). To compare the two distributions, we have transformed the SDSS magnitudes into the R Vega magnitudes using equation (8).

In the case of star counts (Fig. 12), the counts from our survey and SDSS agree very well between $R = 18$ and $R = 22$. For magnitudes brighter than $R = 18$, most of the stars detected in our survey are saturated and do not appear in our catalogs. Star counts drop very rapidly for magnitudes fainter than $R = 24$, since the profile criterion used for the star-galaxy separation fails for faint objects. For comparison, we show in Figure 12 the star counts in the ELAIS field and those in the *Chandra* field (Groenewegen et al. 2002). These fields, which lie at higher Galactic latitudes, are, as expected, less populated by stars.
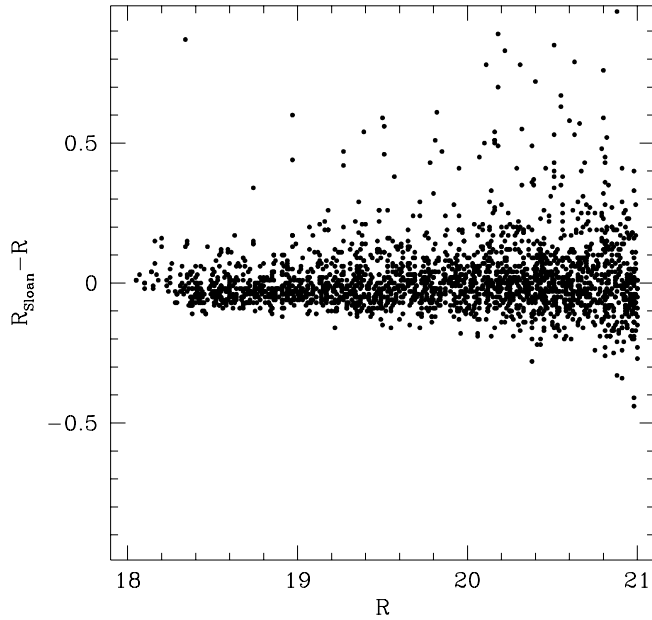
FIG. 10.—Comparison between the R magnitudes of stars in common with the Sloan survey in field FLS 18 as a function of the R magnitude (Vega system).
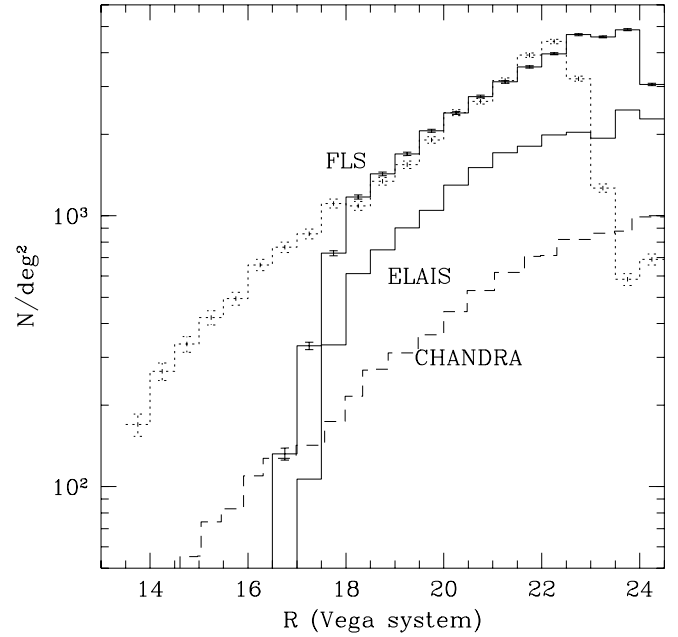

FIG. 12.—Star counts in the central square degree of the FLS region from our R images (*solid lines*) and SDSS (*dotted line*). For comparison, the dashed line refers to the counts in the Chandra Deep Field South region (Groenewegen et al. 2002).

To evaluate the variation in the number counts due to the varying observing conditions, we have computed the counts for each of the subfields in the FLS field. In Figure 13 we show these counts, as well as the median counts with error bars corresponding to the standard deviation as measured from the observed scatter in the counts of the different subfields. One can easily see that a few subfields (Nos. 4, 7, 8, 15, and 26) are less deep than the others, as expected from the quantities measured in Table 5. Fortunately, these fields are external and have been only partially covered by *Spitzer* observations. The other 20 fields in the FLS are quite homogeneous.

Median counts are then reported in Figure 14 to compare with the results from other surveys. The dotted line corresponds to the counts from SDSS in the FLS field (Stoughton et al. 2002) computed by transforming the SDSS magnitudes into Vega R magnitudes using the relationship in equation (8). The points from the general SDSS counts (Yasuda et al. 2001) have been approximately transformed using the relationship from Fukugita et al. (1995), assuming that galaxies have $R-r'$ colors typical of spirals at redshifts of $0.2-0.5$. At the faint

FIG. 11.—Offsets between our and Sloan magnitudes for stars with $18 < R < 21$ in the various FLS fields. The average difference is -0.007 ± 0.016.
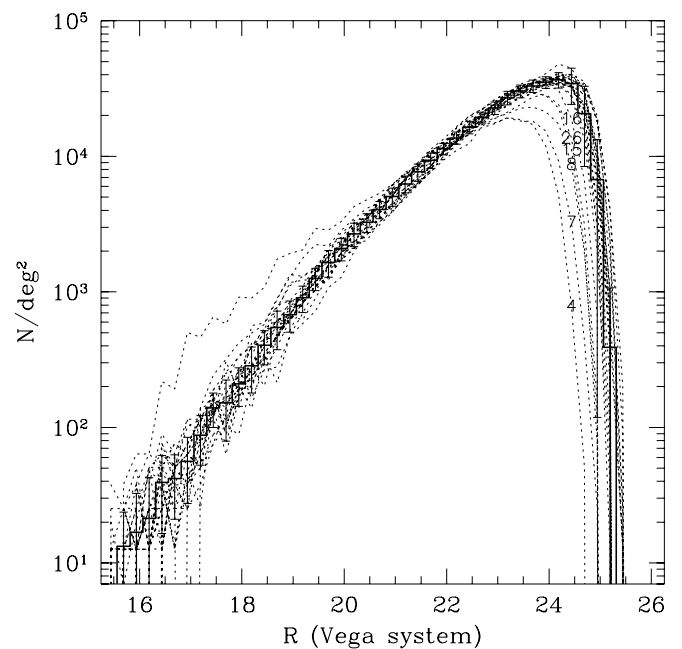
FIG. 13.—Galaxy counts in the various FLS subfields. The numbers refer to the FLS subfields with shallowest depths.
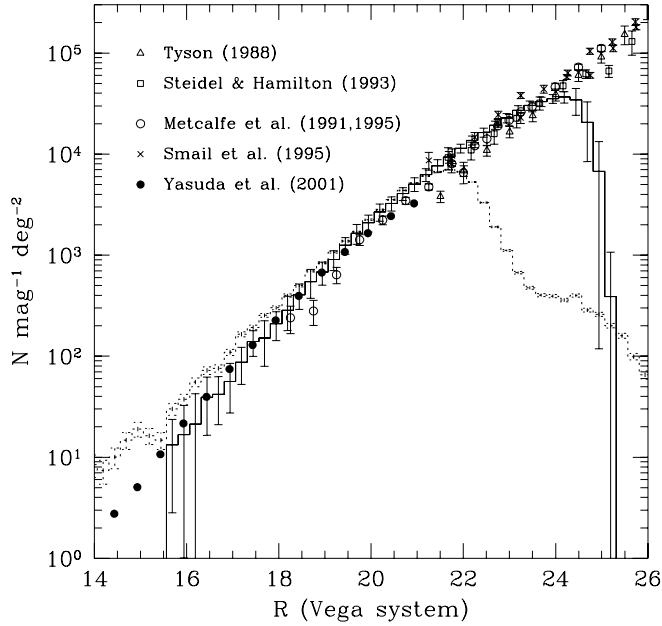
FIG. 14.—Galaxy counts in the FLS region from our *R* images (*solid line*) and SDSS (*dotted line*). Results from counts in other sky regions are overplotted.
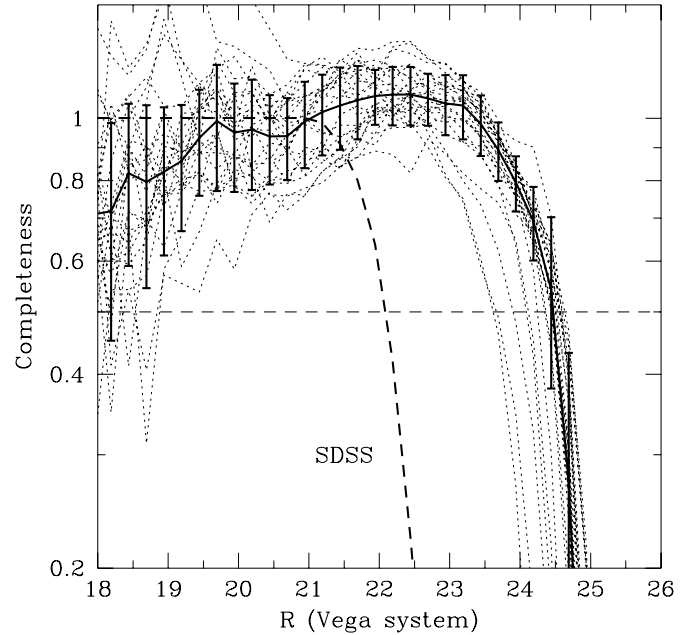

FIG. 15.—Ratio between the number of galaxies in our FLS survey and that of SDSS in the same region for $R < 21$ and that of median counts from several deep surveys at $R > 21$. Dotted lines show the completeness of single FLS subfields, while the dashed line shows the completeness of SDSS in the FLS field.

end of the counts, results from several deep surveys are reported.

As an estimate of the completeness of our images, we have compared our counts with the SDSS counts in the FLS field for $R < 21$ and with median counts from the other deep surveys at magnitudes fainter than $R = 21$. In Figure 15, we show the completeness of the single subfields in the FLS field (*dotted lines*) and those of the global field and the Sloan survey (*solid and dashed thick lines, respectively*). Our survey is deeper than the SDSS data by almost 3 mag. It is 50% complete around $R = 24.5$. This estimate is conservative, since the number of spurious detection at $R = 24.5$ is still relatively small (less than 0.5%). Finally, for magnitudes brighter than $R = 18$ the galaxy catalogs are slightly incomplete, since a few extended objects are saturated.

7. SUMMARY

A deep NOAO/KPNO survey in the *R* band has been carried out to observe a field of more than 9 square degrees centered at $17^h18^m00^s$, $+59°30'00''$ (J2000), aimed to find optical counterparts for the First-Look Survey, which surveys seven different infrared wavelengths with the instruments IRAC and MIPS using the *Spitzer Space Telescope*. Another 2.3 deg^2 has been surveyed in the ELAIS-N1 region, which will be observed in the *Spitzer* SWIRE Legacy survey. This paper describes the observation strategy, the data reduction, and the products that are publicly available to the astronomical community on the World Wide Web at the *Spitzer* Science Center and the NOAO Science Archive.

The overall quality of the data is good and homogeneous: the average seeing is $1''1$ and typically varies between $0''9$ and $1''2$. The limiting magnitude of the images, measured inside an aperture of 1.35 FWHM, for which the signal-to-noise ratio is maximal, is around $R = 25.5$ at 5 σ, deep enough to detect

optical counterparts for a substantial fraction of the new *Spitzer*-selected objects.

An average number of 35,000 extragalactic sources are detected in each subfield ($40' \times 40'$, approximately), with a 50% completeness limit of $R = 24.5$ as deduced by comparing the counts with other deeper surveys. Images and catalogs are available to the astronomical community along with the first release of the FLS infrared data, to exploit in the best way the wealth of extragalactic data expected from the new infrared observatory *Spitzer*.

REFERENCES

Abazajian, K., et al. 2003, AJ, 126, 2081
Bertin, E., & Arnouts, S. 1996, A&AS, 117, 393
Brown, M. J. I., Dey, A., Jannuzi, B. T., Lauer, T. R., Tiede, G. P., & Mikles, V. J. 2003, ApJ, 597, 225
Condon, J. J., Cotton, W. D., Yin, Q. F., Shupe, D. L., Storrie-Lombardi, L. J., Helou, G., Soifer, B. T., & Werner, M. W. 2003, AJ, 125, 2411
Dickinson, M., & Giavalisco, M. 2003, in The Mass of Galaxies at Low and High Redshift, ed. R. Bender & A. Renzini (Berlin: Springer), 324
Dole, H., et al. 2001, BAAS, 33, 1382
Fazio, G. G., et al. 1998, Proc. SPIE, 3354, 1024
Fukugita, M., Shimasaku, K., & Ichikawa, T. 1995, PASP, 107, 945
Gallagher, D. B., Irace, W. R., & Werner, M. W. 2003, Proc. SPIE, 4850, 17
Groenewegen, M. A. T., et al. 2002, A&A, 392, 741
Hogg, D. W., Blanton, M. R., Finkbeiner, D. P., Padmanabhan, N., & Schlegel, D. J. 2004, in preparation
Irwin, M. J. 1985, MNRAS, 214, 575
Jannuzi, B. T., & Dey, A. 1999, in ASP Conf. Ser. 191, Photometric Redshifts and High Redshift Galaxies, ed. R. J. Weymann, L. J. Storrie-Lombardi, M. Sawicki, & R. J. Brunner (San Francisco: ASP), 111
Jannuzi, B. T., et al. 2004, in preparation
Kessler, M. F., et al. 1996, A&A, 315, L27

Kron, R. G. 1980, ApJS, 43, 305
Landolt, A. U. 1992, AJ, 104, 340
Lonsdale, C. J., et al. 2003, PASP, 115, 897
Metcalfe, N., Shanks, T., Fong, R., & Jones, L. R. 1991, MNRAS, 249, 498
Metcalfe, N., Shanks, T., Fong, R., & Roche, N. 1995, MNRAS, 273, 257
Monet, D., et al. 1998, USNO-A2.0 (Flagstaff: US Nav. Obs.)
Muller, G. P., Reed, R., Armandroff, T., Boroson, T. A., & Jacoby, G. H. 1998, Proc. SPIE, 3355, 577
Oliver, S., et al. 2000, MNRAS, 316, 749
Rieke, G. H., Young, E. T., Rivlis, G., & Gautier, T. N. 1996, BAAS, 28, 1274
Schlegel, D. J., Finkbeiner, D. P., & Davis, M. 1998, ApJ, 500, 525
Smail, I., Hogg, D. W., Yan, L., & Cohen, J. G. 1995, ApJ, 449, L105
Smith, J. A., et al. 2002, AJ, 123, 2121
Soifer, B. T., Neugebauer, G., Beichman, C. A., Houck, J. R., & Rowan-Robinson, M. 1983, Proc. SPIE, 428, 297
Steidel, C. C., & Hamilton, D. 1993, AJ, 105, 2017
Stoughton, C., et al. 2002, AJ, 123, 485
Tyson, J. A. 1988, AJ, 96, 1
Valdes, F. G. 2002, in Automated Data Analysis in Astronomy, ed. R. Gupta, H. P. Singh, & C. A. L. Bailer-Jones (New Delhi: Narosa), 309
Yasuda, N., et al. 2001, AJ, 122, 1104